

Coordination engineering in Nd³⁺-doped silica glass for improving repetition rate of 920-nm ultrashort-pulse fiber laser

Yafei Wang,^{a,†} Yinggang Chen,^{a,b,†} Shikai Wang,^{a,*} Meng Wang,^a Lei Zhang,^{©,a} Suya Feng,^a Fei Yu,^{a,c} Guoping Dong,^d Lei Wen,^a Danping Chen,^{©,a} Chunlei Yu,^{a,c,*} and Lili Hu^{a,c,*}

^aChinese Academy of Sciences, Shanghai Institute of Optics and Fine Mechanics, Key Laboratory of Materials for High Power Laser, Shanghai, China

^bUniversity of Chinese Academy of Sciences, Beijing, China

^cUniversity of Chinese Academy of Sciences, Hangzhou Institute for Advanced Study, Hangzhou, China

^dSouth China University of Technology, School of Materials Science and Engineering, State Key Laboratory of Luminescent Materials and Devices, Guangzhou, China

Abstract. Ultrashort pulses at 920 nm are a highly desired light source in two-photon microscopy for the efficient excitation of green fluorescence protein. Although Nd³⁺-doped fibers have been utilized for 920-nm ultrashort pulse generation, the competitive amplified spontaneous emission (ASE) at 1.06 μm remains a significant challenge in improving their performance. Here, we demonstrate a coordination engineering strategy to tailor the properties of Nd³⁺-doped silica glass and fiber. By elevating the covalency between Nd³⁺ and bonded anions via sulfur incorporation, the fiber gain performance at 920 nm is enhanced, and 1.06-μm ASE intensity is suppressed simultaneously. As a result, the continuous-wave laser efficiencies and signal-to-noise ratio at 920 nm by this fiber are significantly enhanced. Importantly, the stable picosecond pulses at 920 nm are produced by a passive mode-locking technique with a fundamental repetition rate up to 207 MHz, which, to the best of our knowledge, is the highest reported repetition rate realized by Nd³⁺-doped silica fibers. The presented strategy enriches the capacity of Nd³⁺-doped silica fiber in generating 920-nm ultrashort pulses for application in biophotonics, and it also provides a promising way to tune the properties of rare-earth ion-doped silica glasses and fibers toward ultrafast lasers.

Keywords: rare-earth-doped fiber; ultrashort pulse; high repetition rate; fiber laser.

Received Jul. 11, 2023; revised manuscript received Sep. 2, 2023; accepted for publication Sep. 6, 2023; published online Sep. 28, 2023.

© The Authors. Published by SPIE and CLP under a Creative Commons Attribution 4.0 International License. Distribution or reproduction of this work in whole or in part requires full attribution of the original publication, including its DOI.

[DOI: [10.1117/1.APN.2.6.066002](https://doi.org/10.1117/1.APN.2.6.066002)]

1 Introduction

Owing to their excellent performance in terms of short pulse duration and high peak power, ultrashort pulse lasers have gained much attention in the fields of fiber-optics communication, biophotonics, and industrial processing.^{1–8} Recently, because of the advantages of compactness, robustness, and freedom from maintenance over conventional solid-state lasers,^{9–13} fiberized ultrashort pulses operating in the wavelength

range from 900 to 950 nm produced by passive mode-locking techniques have become highly desirable for use in two-photon bioimaging (TPM) systems for the efficient excitation of green fluorescent proteins and their variants.^{14–18} Combined with nonlinear frequency conversion, 1.0-μm Yb³⁺-doped,¹² 1.5-μm Er³⁺-doped,¹⁹ and 1.9-μm Tm³⁺-doped^{10,13} ultrashort fiber lasers have been utilized to achieve 900- ~950-nm ultrashort pulses, which have propelled the advances of TPM systems, with the only drawback being the reduced all-fiber configuration as a result of using these additional nonlinear media. As a comparison, the direct generation of ultrashort pulses at 920 nm using Nd³⁺-doped fibers is a more straightforward method^{9,20–24} and has attracted considerable research interest because the emission

*Address all correspondence to Shikai Wang, woshiwsk@163.com; Chunlei Yu, sdyclcy@163.com; Lili Hu, hulili@siom.ac.cn

[†]These authors contributed equally to this work.

of its three-level (${}^4F_{3/2} \rightarrow {}^4I_{9/2}$) transition falls into the 900 to 950 nm wavelength band.

Taking Nd³⁺-doped multicomponent fibers and silica fibers as gain media, ultrafast fiber lasers ranging from 905 to 932 nm have been previously studied using different passive mode-locking techniques, including nonlinear amplification loop mirrors,^{21–23} nonlinear polarization rotation,^{24,25} and semiconductor saturable absorber mirrors (SESAMs).^{26,27} In particular, due to high rare-earth (RE) ions' solubility, these Nd³⁺-doped multicomponent fibers enable gigahertz repetition rate 920 nm ultrashort pulses.^{26–28} Nevertheless, owing to the inherent difference in glass softening temperature and thermal expansion coefficient, the low-loss and high-strength fusion splicing between multicomponent fibers and silica fibers has been an obstacle to their commercialization.²⁹ Furthermore, the low damage threshold of multicomponents is another concern for their long-term running. In terms of practical applications, silica fibers are still an irreplaceable host for RE ion doping in the near-infrared (NIR) region.

However, in terms of Nd³⁺-doped silica fibers, two issues have been limiting the performance improvement of 920 nm ultrashort pulses; taking the pulse repetition rate as an example, it is still well below 100 MHz^{21–25}—much lower than that of these multicomponent fibers,^{26–28} which hardly meets the requirement of TPM imaging speed increase, as higher repetition rates are required to shorten the pixel dwell time via dense two-photon excitation.²⁷ The first issue, generally regarded as the most challenging one, is the competitive 1.06- μm amplified spontaneous emission (ASE) of the four-level transition (${}^4F_{3/2} \rightarrow {}^4I_{11/2}$), which originates from the same upper laser level (${}^4F_{3/2}$) as the 920 nm but with a stronger intensity.^{30,31} This usually develops into noise or even parasitic oscillation that affects the self-starting of the mode-locking process. To weaken the 1.06- μm ASE, W-type Nd³⁺-doped silica fibers are ordinarily adopted because this waveguide structure can induce an effective cutoff wavelength near 1060 nm.^{25,32} Yet, the pulse repetition rate by these W-type fibers, as mentioned above, is limited to relatively low values of <100 MHz.^{22,25} The reason for this repetition rate limitation comes from the second issue—the low RE ion solubility of silica glass, which leads to low pump absorption and optical gain. Co-doping with Al or P is a feasible method to improve the doping level of RE ions in silica glass. However, this method is literally not beneficial for the 0.9- μm laser oscillation when considering the spectral properties because the photoluminescence of Nd³⁺ tends to enhance the 1.06- μm transition probability once these cations are introduced. In addition, the emission peak also exhibits an obvious blueshift, such as shifting from 935 to 900 nm or even shorter after P incorporation,^{33,34} causing deviation of the fiber gain spectrum from the desired wavelength window. How to elevate the 920 nm optical gain and suppress the 1.06- μm ASE in Nd³⁺-doped silica fiber still remains a challenge in improving the 920-nm ultrashort pulse performance.

In this work, we demonstrate a coordination engineering strategy to enhance the gain performance at 920 nm, while suppressing the 1.06- μm ASE intensity of Nd³⁺-doped silica fibers. Sulfur is introduced into the fiber core glass using the modified sol-gel (M-Sol-Gel) method with high-temperature sintering technology, creating a coordinate environment of Nd³⁺ that is more favorable for the three-level transition instead of the four-level transition. As a result, the 920-nm passively mode-locked laser built by this novel Nd³⁺-doped silica fiber yields

a repetition rate over 200 MHz. To the best of our knowledge, the 207 MHz fundamental repetition rate of 920-nm ultrashort pulses reported here is the highest value realized in Nd³⁺-doped silica fibers, which can be a promising light source in high-speed TPM systems.

2 Results and Discussion

2.1 Theoretical analysis by Judd–Ofelt Theory

Manipulating the coordinate environment of RE ions is an effective strategy for achieving desirable optical properties.³⁵ As analyzed in our previous research,³⁶ we detailed in theory the suitable environment favorable for the ${}^4F_{3/2} \rightarrow {}^4I_{9/2}$ transition of Nd³⁺ by the Judd–Ofelt theory. The theoretical spontaneous emission probabilities $A(J \rightarrow J')$ are determined by the following equation:

$$A(J \rightarrow J') = \frac{64\pi^4 e^2}{3h\lambda^3 (2J+1)} \times \frac{n(n^2+2)^2}{9} \times \sum_{t=2,4,6} \Omega_t |\langle \varphi^a | U^{(t)} | \varphi^b \rangle|^2. \quad (1)$$

The fluorescence branching ratio (β_x , $x = {}^4I_{9/2}$, ${}^4I_{11/2}$ or ${}^4I_{13/2}$) for these three transitions of Nd³⁺ is calculated based on spontaneous emission probability as

$$\beta_x = \frac{A(J \rightarrow J')}{\sum_{J'} A(J \rightarrow J')}, \quad (2)$$

where J is the total angular momentum and equals to 3/2 for the transitions from the ${}^4F_{3/2}$ level, J' is the total angular momentum of the lower state and equals to 9/2, 11/2, and 13/2, respectively, λ is the emission peak wavelength, and n is the refractive index. $|\langle \varphi^a | U^{(t)} | \varphi^b \rangle|^2$ ($t = 2, 4, 6$) are the doubly reduced unit tensor operators and independent of the matrix;³⁷ the values are listed in Table 1.

The $|\langle \varphi^a | U^{(2)} | \varphi^b \rangle|^2$ for these three transitions is null, i.e., ($J \rightarrow J'$) are dominated by Ω_4 and Ω_6 as evaluated by Eq. (1). Combined with Eq. (2), it can be derived that the β_x is governed only by the ratio of Ω_4/Ω_6 ; $\beta({}^4I_{9/2})$ will increase only by increasing the Ω_4/Ω_6 while both $\beta({}^4I_{11/2})$ and $\beta({}^4I_{13/2})$ decrease. Consequently, a larger Ω_4 or a smaller Ω_6 is desired for larger $\beta({}^4I_{9/2})$. The Ω_6 is closely linked with the overlap integrals of the 4f and 5d orbitals and decreases as the outermost electron cloud density of Nd³⁺ increases, which can be achieved by increasing the covalency between Nd³⁺ and the bond anion.³⁸ Therefore, the key to enhancing $\beta({}^4I_{9/2})$ is to create a coordinate environment of Nd³⁺ featuring stronger covalency with the bond anion.³⁶

Table 1 The doubly reduced matrix elements of ${}^4F_{3/2} \rightarrow {}^4I_{9/2}$, ${}^4I_{11/2}$, ${}^4I_{13/2}$ transitions, respectively.

Transition	$ \langle \varphi^a U^{(2)} \varphi^b \rangle ^2$	$ \langle \varphi^a U^{(4)} \varphi^b \rangle ^2$	$ \langle \varphi^a U^{(6)} \varphi^b \rangle ^2$
${}^4F_{3/2} \rightarrow {}^4I_{9/2}$	0	0.228	0.055
${}^4F_{3/2} \rightarrow {}^4I_{11/2}$	0	0.142	0.408
${}^4F_{3/2} \rightarrow {}^4I_{13/2}$	0	0	0.209

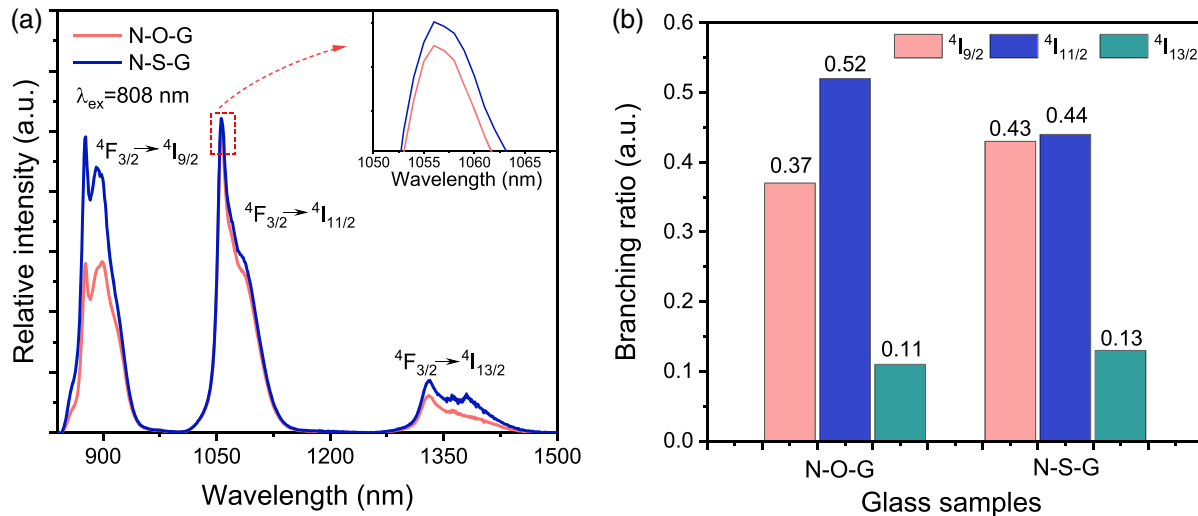


Fig. 1 (a) Emission spectra of N-O-G and N-S-G samples under the 808 nm excitation. Inset is enlarged view of 1.06- μ m emission peak. (b) Calculated fluorescence branching ratios of N-S-G and N-O-G by integrating the peak areas.

2.2 Design of Surrounding Environment of Nd³⁺

Different from multicomponent glasses, the coordination engineering of RE ions in silica-based glasses is challenging because their rigid network limits the components that can be incorporated.²⁹ In this case, we recognize these non-oxygen anions, such as S, can be used as they play the same role as oxygen in silicate glass networks, bridging with cations.³⁹ More importantly, the electronegativity of S (2.5) is much smaller than that of O (3.5); we can evaluate accurately the electronegativity differences of the Nd-S bond (1.3), which is much smaller than that of Nd-O (2.3), given the electronegativity of Nd (1.2). In other words, it can therefore be reasonably deduced that Nd³⁺-doped silica glass would benefit to three-level transition instead of the four-level transition when using sulfur to tailor the coordinate environment of Nd³⁺. Here, we use Nd₂S₃ as a dopant to create such an environment for Nd³⁺, and the glass (labeled as N-S-G) was fabricated by our M-Sol-Gel method combined with the high temperature sintering technique,^{40,41} which also permits high doping level and uniform dispersity. Furthermore, Nd₂O₃-doped silica glass, denoted as N-O-G, was also fabricated for comparison.

As shown in Fig. 1(a), the photoluminescence spectra of the emission bands of Nd³⁺ reveal several intriguing features after the introduction of sulfur. First, under the excitation of an 808 nm laser diode (LD), a notable enhancement in the overall NIR emission intensity for N-S-G is observed, and the peak positions keep identical with N-O-G. The second feature is that the increased intensity at 900 nm is much higher than that at 1064 nm. As shown in Fig. 1(b), compared to N-O-G, the $\beta(4I_{9/2})$ of the three-level transition (0.9 μ m) of N-S-G increased from 0.37 to 0.43, while $\beta(4I_{11/2})$ of the four-level transition decreased from 0.52 to 0.44; that is, the $\beta(4I_{9/2})$ of the three-level transition in N-S-G is indeed increased, as expected. The $\beta(4I_{9/2})$ in N-S-G is much higher than that of Nd³⁺-doped silica glasses³⁴ and multicomponent glasses.²⁶ The lifetime of ⁴F_{3/2} level in sample N-S-G also shows a slight increase, from 364 to 373 μ s (Fig. S1 in the [Supplementary Material](#)), showing that no concentration quenching occurs.

To verify that the spectral variation originated from the environment change surrounding Nd³⁺, we first performed the transmission electron microscopy (TEM) analysis combined with energy-dispersive X-ray spectrometry (EDS) to confirm the sulfur was indeed introduced into the silica glass. Figure 2(a) presents the photograph of N-S-G, from which we can observe that the glass sample retains high transmittance and homogeneity. Figures 2(c)–2(g) are the measurement results of TEM. With the addition of Si, Al, O, and Nd, an obvious EDS signal of S is detected in N-S-G; it presents the same distribution characteristics as the other elements, unambiguously showing the presence of sulfur. Furthermore, the electron probe microanalysis (EPMA) mapping analysis of Nd (Fig. S2 in the [Supplementary Material](#)) also presents its uniform distribution at a larger scale. These characteristics of element distribution also confirm the glass homogeneity of the N-S-G sample.

The variation in the environment surrounding Nd³⁺ was further validated by the spectroscopic intensity parameters (Ω_t , $t = 2, 4, 6$) analysis by the above-mentioned Judd–Ofelt theory. Based on the absorption spectra of N-O-G and N-S-G (Fig. S3 in the [Supplementary Material](#)), the Ω_t were derived using the least squares fitting method.³⁶ The low root-mean square deviation, δ_{rms} (10^{-7}), shows the reliability of these parameters. As listed in Table 2, compared to N-O-G, N-S-G has a smaller Ω_6 and larger Ω_4 , i.e., a larger value of Ω_4/Ω_6 , indicating a higher covalence degree between Nd³⁺ and the bonding anion. Furthermore, the Ω_2 for N-S-G is also higher than that of the N-O-G, which also reflects the asymmetry degree around Nd³⁺, and covalence between RE³⁺ and the bonding anions are elevated.³⁴ Combining the aforementioned analyses, we infer that sulfur breaks the Si–O rigid network by replacing some of the oxygen and enters into the direct neighbor coordination with Nd³⁺, creating an environment that is more beneficial to the 0.9- μ m emission.

2.3 Improvement of Fiber and Laser Performance

The key performance that needs to be explored is whether the tailored coordinate environment can be transferred to fiber when

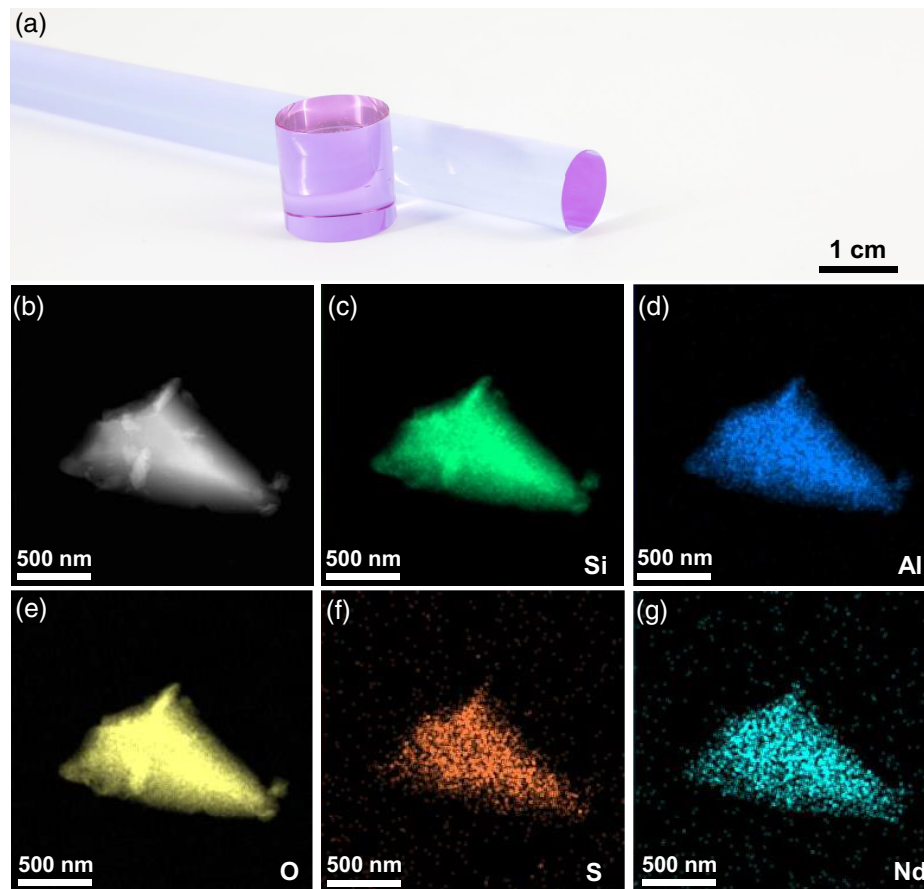


Fig. 2 (a) Photograph of N-S-G sample. (b) TEM image of N-S-G sample. This glass is ground into powder for testing. (c)–(g) EDS mapping analyses of elements of Si, Al, O, S, and Nd, respectively.

Table 2 The calculated Judd–Ofelt intensity parameters (Ω_t , $t = 2, 4, 6$) of N-S-G and N-O-G.

Sample	Ω_2	Ω_4	Ω_6	Ω_4/Ω_6	δ_{rms}
N-S-G	9.46	3.82	3.13	1.22	0.33
N-O-G	8.75	2.09	3.61	0.58	0.42

subjected to a secondary high-temperature process during fiber drawing. Using the well-polished Nd-S-G and Nd-O-G rods as cores, we directly fabricated two standard Nd³⁺-doped silica single-mode fibers, denoted as N-S-F and N-O-F, respectively. The detailed fiber parameters are listed in Table 3. From the fiber refractive index profiles (Fig. S4 in the [Supplementary Material](#)), the numerical apertures (NAs) for N-S-F and N-O-F were calculated to be 0.14 and 0.15, respectively. Moreover, as shown in Figs. 3(a) and 3(b), the fiber absorption coefficient of N-S-F improved; the 808 nm absorption coefficient reached 4.1 dB/cm, which is higher than the 3.7 dB/cm of N-O-F. The differences in the fiber NA and absorption coefficient are additional supports for the different of coordinate environment of Nd³⁺. Furthermore, the preservation of sulfur and its intriguing effect were confirmed by the fiber-forward ASE spectral investigation. As shown in Fig. 3(c), a prominent decrease in

Table 3 Fiber parameters of N-S-F, N-O-F, commercial PM-NDF-5/125 (Nufern), and commercial ND-103 (Coractive).

	N-S-F	N-O-F	PM-NDF-5/125	ND-103
Core diameter (μm)	4	4	5	4.5
Cladding diameter (μm)	125	125	125	125
NA	0.14	0.15	0.15	0.14
Core absorption at 808 nm (dB/cm)	4.1	3.7	4.5	0.36

the 1.06- μm ASE intensity for the N-S-F was observed and, impressively, almost no ASE intensity change or shift around 920 nm occurred. The measurement setup is provided in Fig. S5 in the [Supplementary Material](#). The ASE spectra with linear coordinates [Fig. 3(d)] provide a clearer indication of the weakened 1.06- μm ASE, where the peak intensity of N-S-F at 1062 nm was only 0.63 times that of N-O-F. These data confirm that the created coordinate environment of Nd is preserved in fiber that weakens the 1.06- μm ASE without affecting the required 920 nm. Furthermore, the main reason for 920 nm ASE without exhibiting an obvious improvement, we

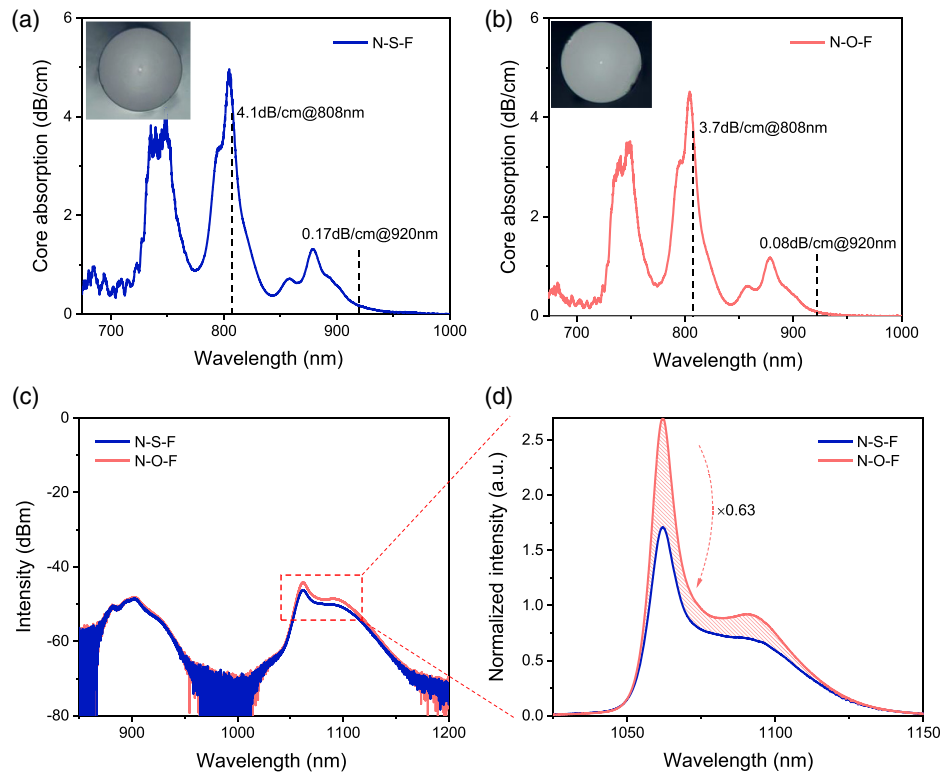


Fig. 3 Absorption spectra of (a) N-S-F and (b) N-O-F. Insets are corresponding fiber cross sections; the fiber diameters are 125 μm . (c) Spectra of forward ASE for N-S-F and N-O-F, core pumped by 200 mW 808 nm LD. (d) Forward ASE spectra in the wavelength region from 1025 to 1150 nm in linear coordinates, which are normalized and take 920 nm intensity as the baseline.

think, is the fiber absorption coefficient at 920 nm also shows a slight increase in N-S-F, as can be seen from Figs. 2(a) and 2(b).

Successful tuning of the fiber ASE properties prompted us to exploit their lasing performance. As presented in Fig. 4(a), we first evaluate the continuous wave (CW) laser efficiency, as it is a direct reflection of the optical gain. The laser cavity was formed by splicing a pair of fiber Bragg gratings (FBGs) centered at 920 nm with a section of Nd³⁺-doped silica fiber. Benefiting from the well-matched fiber NA and core diameter with the passive fiber, the cavity loss was less than 0.2 dB. The reflectivity and 3-dB bandwidth of high-reflection FBG and low-reflection FBG were 99% and 0.5 nm, and 70% and 0.04 nm, respectively. Additionally, two commercial Nd³⁺-doped silica single-mode fibers (Nufern, NDF-PM-5/125 and Coractive, ND103) were also selected for comparison. The detailed fiber properties of the fibers are listed in Table 3. To provided adequate pump absorption, a total of around 40-dB pump absorption was fixed for these four types of fibers. Before injection into an optical spectrum analyzer (OSA), the 920-nm laser powers were attenuated to the same level for better comparison of the laser signal-noise-ratio (SNR) and the 1.06- μm ASE intensity. Figure 4(b) shows the measured laser spectra; clearly, the 920-nm laser were obtained using these four Nd³⁺-doped silica fibers. Detailed laser spectra are provided in Fig. S6 in the [Supplementary Material](#). Among the laser spectra of these four Nd³⁺-doped silica fibers, the 1.06- μm ASE from N-S-F exhibits the lowest intensity, more than 10 dB lower than that of ND103, and thus the 920-nm CW laser by N-S-F presents the highest laser SNR of more than 56 dB. This result

further validates the role of the designed environment of Nd³⁺ in suppressing the 1.06- μm ASE. Moreover, as shown in Fig. 4(c), the laser conversion efficiency by N-S-F also presents remarkable elevation, reaches to 25.4%, compared to the 15.0% for N-O-F, 9.2% for NDF-PM-5/125, and 13.0% for ND103. A maximum slope efficiency of 27.4% was obtained with optimizing N-S-F length (Fig. S7 in the [Supplementary Material](#)). We attributed the significant increase of laser efficiency to the advantage of boosting the radiative transition from $^4F_{3/2}$ level to the ground level ($^4I_{9/2}$) when the transition at 1.06 μm is suppressed after co-doping with sulfur. Moreover, our featured M-Sol-Gel method also permits high Nd³⁺ ion doping with excellent dispersion. It is worth noting that the CW laser operations at 890–910 nm were also achieved by N-S-F (Fig. S8 in the [Supplementary Material](#)), showing a gain bandwidth of at least 30 nm and the potential of tunable fiber laser.

To demonstrate the ability of fiber in generating ultrashort pulses at 920 nm, we selected a linear-cavity passive mode-locking scheme using a commercial SESAM as the mode locker. The experimental setup is illustrated in Fig. 5(a). The SESAM with a 13% modulation depth, 3-ps recovery time, and 15- $\mu\text{J}/\text{cm}^2$ saturable fluence was directly butt-coupled with the fiber end facet. A uniform FBG centered at 920-nm with a 3-dB bandwidth of 1.2 nm was selected to define the laser wavelength and render more oscillating longitudinal modes. The laser cavity is compact, and the shortest length was optimized to ~ 50 cm with a 207-MHz repetition rate picosecond pulse output. We had literally realized a higher repetition rate near 300 MHz by further reducing the cavity length, but its initiating pump

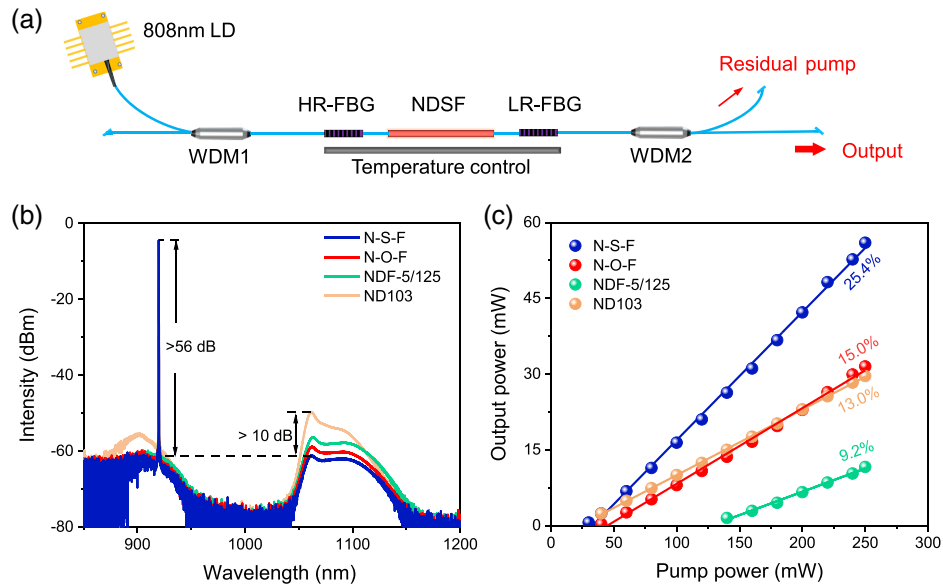


Fig. 4 (a) Experimental setup of CW laser; NDSF, Nd³⁺-doped silica fiber. (b) 920-nm CW laser spectra and (c) output power as a function of pump power by N-S-F, N-O-F, commercial Nufern PM-NDF-5/125, and commercial Coractive ND-103.

threshold was over 300 mW due to the decrease of optical gain, which we think is not beneficial for application, as the maximum power of current 808 nm single-mode LD is around 250 mW. Detailed analyses of this 207-MHz pulse characteristics are shown in Figs. 5(b)–5(f). No obvious intensity fluctuation can be observed either in the 50-ns time span or the wider time span in the typical temporal pulse trains recorded by the oscilloscope [Fig. 5(b)], indicating its temporal stability. The 4.8-ns temporal pulse period, i.e., a 207 MHz repetition rate, conforms to the cavity length and shows the pulse is fundamentally mode-locked. Benefiting from the suppressed 1.06- μ m ASE and boosted fiber gain performance, the repetition rate of N-S-F is much higher than that of the commercial silica fibers.^{24,25} The measured laser spectrum confirms that the laser peak wavelength is at \sim 920 nm with a 3-dB bandwidth of 0.8 nm [Fig. 5(c)], corresponding to a transform-limited sech² pulse width of 1.1 ps. The spectral bandwidth of the laser is narrower than that of the FBG, which may be because not all modes located in the FBG bandwidth are phase-locked, owing to the mode competition.⁴² Considering the gain spectrum of this newly developed fiber is over 30 nm, it is believed broader laser spectrum—supporting narrower transform-limited pulse width—can be enabled if adopting wideband output mirrors, such as fiber-type dielectric film. The inset of Fig. 5(b) shows the spectral evolution in the 2-h time span, during which no wavelength drifting occurred, indicating the long-term stability of the wavelength. The accurate pulse repetition rate is 206.93 MHz rate as recorded using radiofrequency (RF) spectrum [Fig. 5(d)]. The 67.9-dB SNR as well as the clean and flat 5-GHz RF spectrum in the inset of Fig. 5(f) confirms the stability of the mode-locking (ML) state. Assuming a sech²-pulse shape, the pulse duration was determined to be 4.3 ps [Fig. 5(e)], which is larger than the transform-limited pulse width, indicating that the output pulse was chirped. Figure 5(f) shows the average output power as a function of the launched pump power. Self-starting CWML is achieved when the pump power exceeds 175 mW.

The output power is low, only a few milliwatts, which may be caused by the high connection loss between SESAM and N-S-F as well as the fiber reabsorption. The output power would be further amplified by combining our 30/125 μ m Nd³⁺-doped silica fiber.³⁶ These results demonstrate this modified Nd³⁺-doped silica fiber is a suitable medium for producing ultrashort pulses at 920 nm and hold potential as light source in biophotonics.

3 Conclusion

We have presented a strategy of surrounding environment modification using anion to tune the preferable transition of Nd³⁺-doped silica glass. We have shown that sulfur can be stabilized in the fiber and suppresses the competitive 1.06- μ m ASE. Based on this novel Nd³⁺-doped silica fiber, we demonstrate that the CW laser performance at 920 nm can be enhanced, including efficiency and SNR. Especially, the laser efficiency reached up to 27.4%, twice that of commercial Nd³⁺-doped silica fiber. Moreover, this fiber allows for the stable picosecond pulse generation at 920 nm with a high 207 MHz fundamental repetition rate under a proper initiating pump threshold of 175 mW, which is expected to obtain promising applications in biophotonics. The present method also offers an opportunity to tune the properties of RE ion-doped silica glasses and fibers toward ultrafast lasers.

4 Experimental Section

4.1 Sample Fabrication

Nd³⁺-doped silica glasses were prepared using a self-developed M-Sol-Gel method. For the N-O-G sample, high-purity tetraethoxysilane (TEOS, Kermel), AlCl₃·6H₂O (99.9995%, Alfa), and NdCl₃·6H₂O (99.99%, Alfa) were selected as the precursors, and deionized water was added to sustain the hydrolysis reaction. All reagents were mixed and thoroughly stirred at 30°C to form a homogeneous sol, which was then put into an 80°C

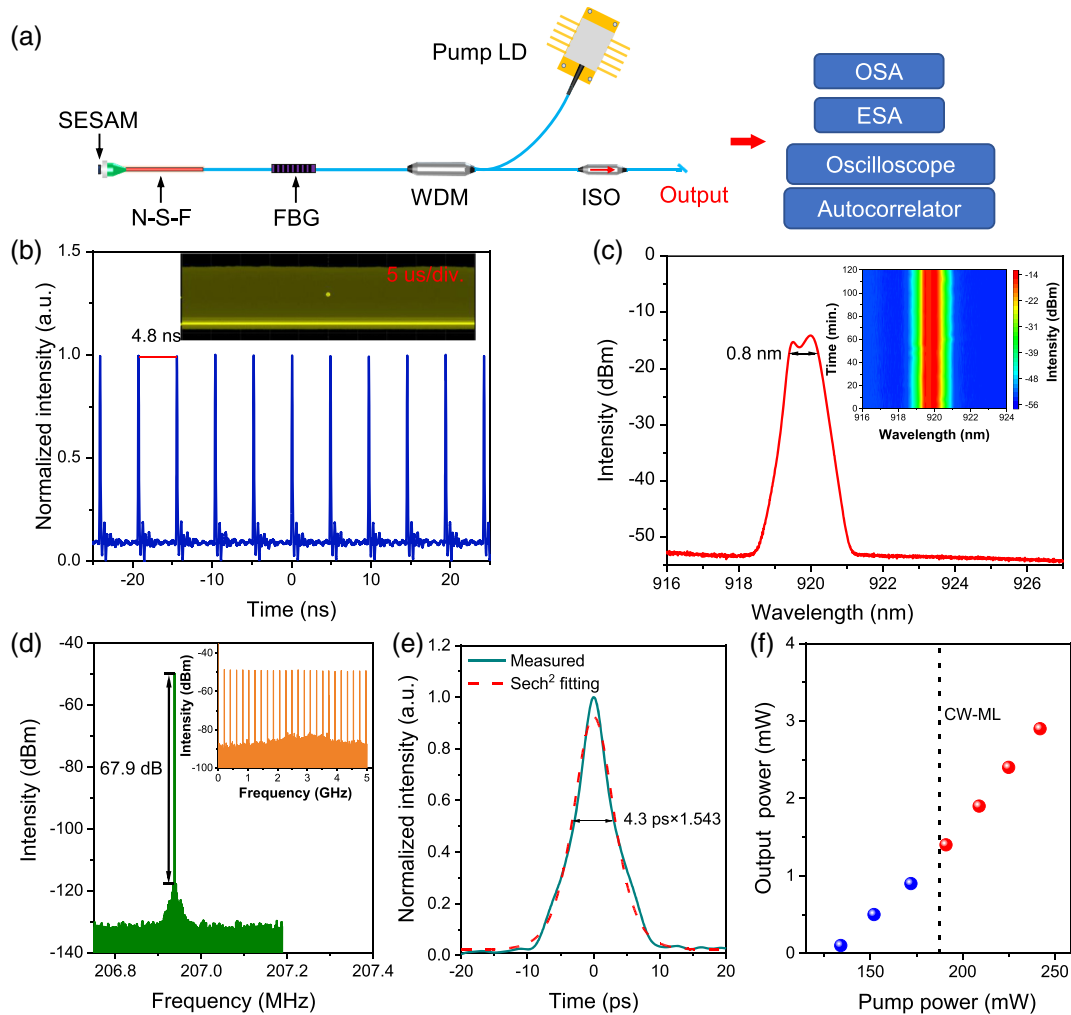


Fig. 5 (a) Experimental setup of the 920 nm passively mode-locked laser using N-S-F. (b) Pulse train in 50-ns time span. Inset is the pulse train over a wider span. (c) Laser spectra of output pulses. Inset is the spectra stability in 2-h time span. (d) RF spectra of the mode-locked pulses. Inset is the RF spectrum in a 5-GHz range. (e) Autocorrelation trace. (f) Output power as a function of launched pump power. OSA, optical spectrum analyzer; ESA, electrical spectrum analyzer; and ML, mode-locking.

water bath for 48 h to obtain millimeter gel particles. In oxygen atmosphere, the gel particles were heated at 1100°C for 5 h to completely remove HCl, moisture, and organic matter. The obtained powder was ball-milled to micrometer level and further melted under vacuum at 1750°C for 2.5 h to form a glass. The fabrication process was the same for the N-S-G sample as for the N-O-G, and sulfur was doped via Nd₂S₃. Argon was also used as the shielding gas atmosphere during the heat treatment process to avoid the oxidation of the sulfur. Both the N-O-G and N-S-G glass samples were doped with Al to improve the dispersity of Nd³⁺ and its doping concentration. The doping levels of Nd and Al in N-O-G and N-S-G were identical, which were 0.3 and 3.0 mol%, respectively. The obtained glasses were cut and well polished to 2-mm thick slices for spectroscopic measurements. The residual glass samples were mechanically shaped into a core-glass rod with a well-polished surface. Then, it was inserted into a silica tube (Heraeus, Suprasil F300) into a preform, which was then drawn into 125- μ m fiber by a drawing tower. The fibers were coated with ultraviolet curing adhesive during the drawing process.

4.2 Characterization

The emission spectra and decay curves of the glass samples were measured on a high-resolution spectrofluorometer (FLS 920, Edinburgh Instruments) with an 808-nm LD as the excitation source. The content of the various elements was measured using an EPMA (JXA8230), with a test error of less than 10%. The refractive indices of the fibers were measured using a fiber index profiler (fiber analysis, IFA-100). The fiber absorption coefficient and propagation loss were measured using a stabilized broadband light source (SLS201L, Thorlabs) and the cutback method. The laser power was measured using a power meter (S145C, Thorlabs) combined with a console (PM100D, Thorlabs). The laser spectra were recorded by an OSA (AQ6374, Yokogawa). The pulse train was measured using a real-time oscilloscope with a bandwidth of 8 GHz (DSOV084A, Keysight) and a photodetector with a span of 5 GHz (DET08CFC, Thorlabs). The RF spectrum was obtained using an electrical spectrum analyzer (N9020B, Keysight). The pulse duration was measured using an autocorrelator (Pulsecheck150, APE).

Availability Statement

The data that support the findings of this article are not publicly available. They can be obtained from the corresponding author upon reasonable request.

Acknowledgments

This study was supported by the International Partnership Program of Chinese Academy of Sciences (Grant No. 20XH1217), the National Natural Science Foundation of China (Grant Nos. 61975216 and 62205356), and the STCSM (Grant No. SKLSFO2022-02). The authors declare no conflict of interest.

References

- P. Grelu and N. Akhmediev, "Dissipative solitons for mode-locked lasers," *Nat. Photonics* **6**(2), 84–92 (2012).
- G. Chang and Z. Wei, "Ultrafast fiber lasers: an expanding versatile toolbox," *iScience* **23**(5), 101101 (2020).
- J. E. Bae et al., "Multi-gigahertz mode-locked femtosecond Yb:KLuW waveguide lasers," *Photonics Res.* **10**(11), 2584 (2022).
- S. Chen et al., "W-type normal dispersion thulium-doped fiber-based high-energy all-fiber femtosecond laser at 1.7 μm ," *Opt. Lett.* **46**(15), 3637–3640 (2021).
- K. Murari et al., "Sub-50 fs pulses at 2050 nm from a picosecond Ho:YLF laser using a two-stage Kagome-fiber-based compressor," *Photonics Res.* **10**(3), 637 (2022).
- M. An et al., "Co-MOFs as emerging pulse modulators for femtosecond ultrafast fiber laser," *ACS Appl. Mater. Interfaces* **14**, 53971–53980 (2022).
- T. Li et al., "Direct generation of 3.17 mJ green pulses in a cavity-dumped Ho³⁺-doped fiber laser at 543 nm," *Photonics Res.* **11**(3), 413 (2023).
- G. Gao et al., "Consecutive 1015–1105-nm wavelength tunable 'figure-of-9' mode-locked Yb: fiber oscillator," *Opt. Lett.* **47**(22), 5869 (2022).
- B. Chen et al., "910 nm femtosecond Nd-doped fiber laser for in vivo two-photon microscopic imaging," *Opt. Express* **24**(15), 16544–16549 (2016).
- R. Dai et al., "High energy (>40 nJ), sub-100 fs, 950 nm laser for two-photon microscopy," *Opt. Express* **29**(24), 38979–38988 (2021).
- K. Charan et al., "Fiber-based tunable repetition rate source for deep tissue two-photon fluorescence microscopy," *Biomed. Opt. Express* **9**(5), 2304–2311 (2018).
- P. Wang et al., "926 nm Yb-doped fiber femtosecond laser system for two-photon microscopy," *Appl. Phys. Express* **12**(3), 032008 (2019).
- H. He et al., "Deep-tissue two-photon microscopy with a frequency-doubled all-fiber mode-locked laser at 937 nm," *Adv. Photonics Nexus* **2**(2), 026001 (2022).
- W. Zong et al., "Miniature two-photon microscopy for enlarged field-of-view, multi-plane and long-term brain imaging," *Nat. Methods* **18**(1), 46–49 (2021).
- W. Zong et al., "Fast high-resolution miniature two-photon microscopy for brain imaging in freely behaving mice," *Nat. Methods* **14**(7), 713 (2017).
- J. Yao et al., "Exploiting the potential of commercial objectives to extend the field of view of two-photon microscopy by adaptive optics," *Opt. Lett.* **47**(4), 989–992 (2022).
- M. Drobizhev et al., "Two-photon absorption properties of fluorescent proteins," *Nat. Methods* **8**(5), 393–399 (2011).
- A. Forli et al., "Two-photon bidirectional control and imaging of neuronal excitability with high spatial resolution in vivo," *Cell Rep.* **22**(11), 3087–3098 (2018).
- C. H. Hage et al., "Two-photon microscopy with a frequency-doubled fully fusion-spliced fiber laser at 1840 nm," *Opt. Lett.* **43**(20), 5098–5101 (2018).
- K. Le Corre et al., "Mode-locked all-PM Nd-doped fiber laser near 910 nm," *Opt. Lett.* **46**(15), 3564–3567 (2021).
- A. A. Mkrtchyan et al., "Nd-doped polarization maintaining all-fiber laser with dissipative soliton resonance mode-locking at 905 nm," *J. Lightwave Technol.* **39**(17), 5582–5588 (2021).
- R. Bechecker et al., "Dissipative soliton resonance in a mode-locked Nd-fiber laser operating at 927 nm," *Opt. Lett.* **44**(22), 5497–5500 (2019).
- S. Wang et al., "Femtosecond all-polarization-maintaining Nd fiber laser at 920 nm mode locked by a biased NALM," *Opt. Express* **29**(23), 38199–38205 (2021).
- X. Gao et al., "Core-pumped femtosecond Nd: fiber laser at 910 and 935 nm," *Opt. Lett.* **39**(15), 4404–4407 (2014).
- K. Qian et al., "Mode-locked Nd-doped fiber laser at 930 nm," *Opt. Lett.* **39**(2), 267–270 (2014).
- Y. Wang et al., "Ultrafast fiber laser at 0.9 μm with a gigahertz fundamental repetition rate by a high gain Nd³⁺-doped phosphate glass fiber," *Opt. Express* **30**(17), 30870 (2022).
- J. Zhang et al., "Watt-level gigahertz femtosecond fiber laser system at 920 nm," *Opt. Lett.* **47**(19), 4941 (2022).
- Y. Wang et al., "Efficient three-level continuous-wave and GHz passively mode-locked laser by a Nd³⁺-doped silicate glass single mode fiber," *Opt. Express* **31**(8), 13307–13316 (2023).
- W. C. Wang et al., "Recent advances in soft optical glass fiber and fiber lasers," *Prog. Mater. Sci.* **101**, 90–171 (2019).
- P. H. Pax et al., "Scalable waveguide design for three-level operation in Neodymium doped fiber laser," *Opt. Express* **24**(25), 28633–28647 (2016).
- A. Wang, A. K. George, and J. C. Knight, "Three-level neodymium fiber laser incorporating photonic bandgap fiber," *Opt. Lett.* **31**(10), 1388–1390 (2006).
- I. A. Bufetov et al., "Efficient 0.9- μm neodymium-doped single-mode fibre laser," *Quantum Electron.* **33**(12), 1035–1037 (2003).
- S. Fu et al., "Single-frequency Nd³⁺-doped phosphate fiber laser at 915 nm," *J. Lightwave Technol.* **39**, 1808–1813 (2020).
- K. Arai et al., "Aluminum or phosphorus co-doping effects on the fluorescence and structural properties of neodymium-doped silica glasses," *J. Appl. Phys.* **59**(10), 3430–3436 (1986).
- S. Zhou et al., "Topological engineering of glass for modulating chemical state of dopants," *Adv. Mater.* **26**(47), 7966 (2014).
- Y. Chen et al., "High-power lasing at \sim 900 nm in Nd³⁺-doped fiber: a direct coordination engineering approach to enhance fluorescence," *Optica* **10**(7), 905 (2023).
- W. T. Carnall, P. R. Fields, and K. Rajnak, "Electronic energy levels in the trivalent lanthanide aquo ions. I. Pr³⁺, Nd³⁺, Pm³⁺, Sm³⁺, Dy³⁺, Ho³⁺, Er³⁺, and Tm³⁺," *J. Chem. Phys.* **49**(10), 4424–4442 (2003).
- S. Tanabe et al., "Correlation between 151Eu isomer shift and Judd-Ofelt parameters of Nd³⁺ ions in phosphate and silicate laser glasses," *Phys. Rev. B* **48**(14), 10591–10594 (1993).
- A. Hayashi et al., "Structural investigation of 95(0.6Li₂S_{0.4}Si₂)5Li₄SiO₄ oxysulfide Glass by using X-ray photoelectron spectroscopy," *J. Am. Ceram. Soc.* **81**(5), 1305–1309 (2005).
- F. Wang et al., "Manipulating refractive index, homogeneity and spectroscopy of Yb³⁺-doped silica-core glass towards high-power large mode area photonic crystal fiber lasers," *Opt. Express* **25**(21), 25960–25969 (2017).
- Y. Chen et al., "Nd³⁺-doped silica glass and fiber prepared by modified sol-gel method," *Chin. Opt. Lett.* **20**(9), 091601 (2022).
- W. Li et al., "0.017 nm, 143 ps passively mode-locked fiber laser based on nonlinear polarization rotation," *Opt. Lett.* **48**(10), 2676–2679 (2023).

Biographies of the authors are not available.